Journal of Energy Storage 99 (2024) 113329

Contents lists available at ScienceDirect

Journal of Energy Storage

journal homepage: www.elsevier.com/locate/est

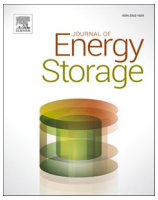

Research papers

Cobalt-free cathodes and silicon thin-film anodes towards high-capacity solid-state batteries

Ryan Brow [a,*], Zachary Berquist [b,c], Steven Lee [d], Trevor Martin [b,c], Lydia Meyer [a], Maxwell Schulze [a], Avtar Singh [a], Ryan Tancin [c], Glenn Teeter [c], Gabriel Veith [e], Bertrand J. Tremolet de Villers [c], Andrew Colclasure [a,*], Arumugam Manthiram [d,*]

[a] Center for Integrated Mobility Sciences, National Renewable Energy Laboratory, Golden, CO 80401, USA
[b] Chemistry and Nanoscience Center, National Renewable Energy Laboratory, Golden, CO 80401, USA
[c] Materials Science Center, National Renewable Energy Laboratory, Golden, CO 80401, USA
[d] Science and Engineering Program and Texas Materials Institute at University of Texas at Austin Austin, TX 78712, USA
[e] Chemical Sciences Division, Oak Ridge National Laboratory, Oak Ridge, TN 37831, USA

ARTICLE INFO

Keywords:
All-solid-state battery
No-cobalt cathode
Nickel-rich cathode
Pure silicon anode
Argyrodite
Pressure

ABSTRACT

This study provides a comprehensive analysis of a novel battery system, which integrates a high-loading (~5 mAh/cm^2) cobalt-free cathode composed of lithium nickel manganese aluminum oxide ($LiNi_{0.9}Mn_{0.05}Al_{0.05}O_2$, NMA) into an all-solid-state cell for the first time. The argyrodite (Li_6PS_5Cl) solid electrolyte is used in conjunction with a 99 wt% silicon thin-film anode. Room temperature discharge capacities of >210 mAh/g_{NMA} and > 170 mAh/g_{NMA} were achieved at cycling rates of 0.05C and 0.25C, respectively. Electrochemical impedance spectroscopy measurements, taken during the first cycle detail onset of electrolyte degradation, lithiation of the silicon anode, and the change in charge transfer kinetics as a function of cell voltage. Raman, Fourier Transform Infrared, and X-ray photoelectron spectroscopy are used to identify the argyrodite degradation products that form in the catholyte on cycling, unveiling lithium carbonate as a potential source of oxygen-related degradation commonly alluded to in literature. Furthermore, high cell stack pressure, 350 MPa during fabrication, led to fracturing and pulverization of some cathode particles.

1. Introduction

In the quest to increase the energy density of electrochemical energy storage devices, all-solid-state batteries (ASSBs) are emerging as a potential contender [1]. Of the solid electrolyte materials, the argyrodite family of sulfur-based electrolytes (Li_6PS_5X where X = Cl, Br, or I) is one of the front runners in development. Argyrodite ASSBs offer a promising avenue towards higher energy density and longer lifespans [2]. However, the highest energy density ASSB architectures often employ cobalt containing cathode materials, which impedes the likelihood of their widespread use due to elemental scarcity and supply chain constraints [3,4]. Moreover, cell architectures with high energies often employ lithium metal anodes which cause instability when coupled with the argyrodite solid electrolytes that have a relatively small electrochemical stability windows [5]. Herein, we report a new ASSB cell configuration that addresses both limitations by using a no-cobalt cathode material and a less-reactive silicon anode.

The shift towards low-cobalt, nickel-rich transition metal layered oxides in cathodes is driven by their superior energy density and lower cost than their cobalt-rich counterparts. These materials, however, grapple with problems like cathode-electrolyte interface instability and lack of consistent mechanical contact between the cathode and electrolyte particles when cycled in solid-state cells [6]. Inconsistent mechanical contact can partially explain the large range in reported cathode utilization in solid-state cell values across the literature [7–9]. The cathode utilization can decrease further on cycling during which nickel-rich cathode materials experience a “c-axis collapse” above 4.2 *V* (all voltages are versus lithium metal unless stated otherwise) [10]. Furthermore, cathode cracking can occur when using the energy-dense nickel-rich cathodes, which can electrically and ionically isolate the now detached particles. While pre-cracking and coating these nickel-rich cathodes has shown some promise in limiting particle isolation in

* Corresponding authors.
E-mail address: Ryan.Brow@nrel.gov (R. Brow).

https://doi.org/10.1016/j.est.2024.113329
Received 9 May 2024; Received in revised form 5 August 2024; Accepted 10 August 2024
Available online 17 August 2024

liquid cells, this method has yet to be explored thoroughly in solid-state cells [10]. This study is the first to use cobalt-free, $LiNi_{0.9}Mn_{0.05}Al_{0.05}O_2$ (NMA) cathode, which demonstrates excellent specific capacity (230 mAh/g) and high cycle-life retention in liquid-electrolyte-based cells, in a ASSB [11].

Lithium metal, despite its high energy density, faces challenges like dendrite growth and aggressive electrolyte reduction when used in solid-state batteries [12]. Due to the difficulty in using lithium metal anodes, silicon anodes have gained great interest because of their high theoretical capacity, nearly ten times that of traditional graphite anodes [13]. The lithium alloying potentials with silicon are in the range of a few hundred mV above lithium plating potentials, meaning the issue of lithium dendrites causing internal short circuiting through the solid-state electrolyte separator can potentially be avoided. Silicon's high lithiation capacity theoretically also allows high energy densities close to those achievable only with lithium metal anodes, a performance metric that other intercalation style anodes such as graphite will always fall short of. Silicon anodes have also demonstrated improved electrochemical stability against the sulfide-based argyrodite solid electrolytes and are not prone to dendrite formation, thereby circumventing the lithium metal interfacial instability issues that have been reported previously [12]. The main obstacle with silicon is its significant volume expansion during lithiation, which can lead to mechanical degradation and reduced silicon-electrolyte contact [14]. However, the high stack pressures typical of solid-state batteries may help overcome the volumetric changes of silicon anodes by maintaining silicon-electrolyte contact [15]. Meng et al. have demonstrated phenomenal performance of a 99 wt% micron-sized silicon anode which greatly limited anode/electrolyte contact area [16]. This cell design allows for the use of high loading anode electrodes without the need for composites. While the use of silicon anodes can eliminate the electrolyte's exposure to the reducing potential of lithium metal, it is still an electronically conductive surface at potentials below argyrodite's stability window.

Deiseroth et al. are typically credited with first proposing lithium-ion substitution into the Ag_8GeS_6 argyrodite structure, yielding Li-ion electrolytes with conductivities close to their liquid counterparts, in the range of 10^{-2} to 10^{-3} $S\,cm^{-1}$ [17]. Argyrodites electrolytes Li_6PS_5X (X = Cl, Br, I) have a face-centered cubic $F\bar{4}3m$ symmetry in which the sulfur and halide anions form the cubic lattice while the PS_4^{3-} tetrahedra occupy the octahedral sites. The room temperature transference number is close to 1, and the ionic conductivity of crystalline Li_6PS_5Cl (LPSC) is 1.9×10^{-3} $S\,cm^{-1}$ [18]. Argyrodites possess greater ductility than many of the oxide-based solid electrolytes, allowing for better particle-particle contact in the cell. However, these systems still suffer from less-than-ideal lithium transport, require high fabrication pressures, and have narrow electrochemical stability windows [5].

Although the argyrodite materials contain great promise, three primary challenges standout: an inability to maintain cathode-electrolyte contact on cycling, a small electrochemical stability window, and dendrite formation (the latter two mechanisms may be related in some cases).

- *Mechanical contact* – All solid electrolytes encounter the issue of maintaining solid-solid contact with cathode and anode particles. This can be viewed from the perspective of a mismatch of mechanical properties such as Young's modulus and hardness (the sulfide's Young's modulus and hardness are 20 GPa and 2 GPa where a typical transition metal oxide cathode's are approximately 100 and 20 GPa respectively) [19]. An additional issue is the solid-state electrolyte's inability to deform properly to accommodate the volume changes in cathode active materials on cycling. These values can be as high 7 % for LFP and single crystalline nickel-rich cathodes at top-of-charge [19]. This can lead to a dramatic reduction in the cathode-electrolyte contact. Consequently, there is a hefty increase in overall cell resistance (~130 $\Omega{\cdot}cm^{-2}$) [20]. To alleviate this issue, large fabrication (>350 MPa) and cycling pressures (>10 MPa) are often used to maintain intimate contact.

- *Stability window* – As discussed above, the argyrodite electrolytes suffer from a narrow electrochemical stability window (~1.07–2.01 *V*) [21]. This creates highly resistive electrolyte decomposition interphases with both the cathode and anode. Below 1.7 *V*, the argyrodite material forms P, Li_2S and LiCl. Predictions made via Density-functional theory (DFT) suggest that P is further reduced to form Li_3P down to 0.8 V. This is set to occur via the decomposition of the lithiated $Li_{11}PS_5Cl$ phase which, has very low activation energy for decomposition [22]. This interphase at the anode can have ionic conductivities as low as 3.2×10^{-6} $S\,cm^{-1}$ [23] and can be 10–250 nm thick, depending on the method used to measure it [24,25].

  The oxidation products of the argyrodite LPSC at the cathode interface are thought to be Li_3PS_4, S and LiCl, where Li_3PS_4 can be further oxidized above 2.4 *V* to form P_2S_5 and then to $P_2S_7^{4-}$ above 2.9 V [26]. However, there is some debate about whether LPSC undergoes direct decomposition or an indirect decomposition via the delithiated Li_4PS_5Cl phase. Somewhat interestingly, some studies report sulfate or sulfite species near the cathode-LSPC interface, and others do not [27]. This will be discussed in greater detail below. There is some evidence to suggest that there can be polysulfides formed via polymerization of the anions, which can form P–[S]*n*–P-type anions species [28]. Additional decomposition products involving the cathode's transition metals (transition-metal sulfides, phosphides, and chlorides) have been detected using ToF-SIMS; however, they are assumed to play an insignificant role in capacity fade or increased cell resistance [28].

- *Dendrite formation* – Two types of dendrite-like formations have been identified, soft and hard shorts. Hard shorts occur when there is a complete electronic path between electrodes which, in ASSBs, is thought to usually occur via a lithium dendrite. These shorts are typically easy to identify since they often cause a dramatic decrease in the overall cell potential, causing the cell to behave more as a resistor [29]. Unfortunately, soft shorts are more difficult to recognize. Soft shorts describe a phenomenon where a moss-like, submicron growth of lithium dendrites forms in the SSE layer. They are difficult to recognize because cells experiencing them often do not lose their overall cell potential as the structures are too fine to pass high currents. It is thought that this sea of fine dendrites experiences electromigration (or perhaps thermal cutoff) on contact with the terminal electrode, disrupting the direct electron path [30]. This mechanism makes identifying soft shorts in full cells challenging and has possibly led to the publication of data from cells that contain them, unbeknownst to the authors [31].

Several factors seem to control for the prevalence of dendritic growth, including the Young's modulus of the SSE [32], the size and orientation of grain boundaries [33], electrolyte degradation that is conducive to lithium metal deposition, current density [34], temperature, and external pressure applied to the cell [35]. Phase field simulations were used to understand the relationship between continuous soft shorts in SSEs and external pressure. These studies suggest that cells under higher external pressure were more likely to form dead lithium, dendrites that are no longer connected to either electrode [30].

The transition from lab-scale prototypes to commercial-scale production of solid-state batteries is laden with challenges. Key areas of focus include developing cost-effective, scalable manufacturing processes that can maintain low defect density, great active material-SSE particle contact at low pressure, and low overall cell resistance both pre and post-cycling. Moreover, the pressures required to accomplish reasonable cell capacities at the lab scale (often >10 MPa) are unacceptable at the commercial scale. These high pressures require bulky cell enclosures and may induce cathode fracturing at high enough pressures.

Efforts and methods must be pursued to minimize the overall fabrication pressure used to consolidate cell stacks.

The three main issues facing solid-state cells can be influenced greatly by the manufacturing process used. In addition, large scale manufacturing involves processes that can complicate the already difficult to fabricate lab-scale prototypes (pellet cells) including the inclusion of binders [36], solvents [37], and wet or dry film deposition [38]. For LPSC, this must all take place in a dry room environment since it readily hydrolyzes to form toxic H_2S in air [39]. Additionally, since oxygen contamination in the electrolyte provides an additional decomposition pathway towards sulfate and sulfites, best practice may be to perform all of the LPSC processing in an inert environment [40].

We report, for the first time, an NMA–silicon hybrid cell that has high utilization, high loading, low impedance, and reasonable capacity retention. Specifically, this work demonstrates a novel ASSB cell configuration that addresses lithium metal anode instabilities by utilizing a silicon anode and that avoids cobalt scarcity issues by incorporating a cobalt-free cathode material. Furthermore, we discuss the degradation mechanisms of this cell architecture in detail using a variety of spectroscopic techniques which to our knowledge have not been reported previously for a no-cobalt NMC-type cathode chemistry. This was accomplished by using an extended mixing regimen of the various catholyte components (55 wt% NMA, LPSC argyrodite 44 wt%, conductive carbon 1 wt%) and continuous pressure between the fabrication and electrochemical cycling steps. The anode is an impressive 99 wt% thin-film silicon anode with 1 wt% binder. Several characterization techniques suggest that the nickel-rich NMA does not experience additional cathode-electrolyte degradation processes compared to those found in other nickel-rich NMC-type cathodes and lithium carbonate in the catholyte may be the source of oxygen-related phosphate and sulfate formation.

2. Methods and materials

2.1. NMA synthesis

Cells constructed and tested in this manuscript utilized $LiNi_{0.9}Mn_{0.05}Al_{0.05}O_2$ (NMA) as the cathode active material. NMA was synthesized in the following procedure: First, the spherical $Ni_{0.9}Mn_{0.05}Al_{0.05}(OH)_2$ precursor with a diameter of 10–12 μm was synthesized via coprecipitation as described in a previous publication [11]. Aqueous solutions of $NiSO_4{\cdot}6H_2O$, $MnSO_4{\cdot}H_2O$, and $Al(NO_3)_3{\cdot}9H_2O$ were prepared with appropriate molar ratios and pumped into a 10 L continuously stirred tank reactor under a nitrogen atmosphere. Aqueous solutions of KOH and NH_4OH were simultaneously fed into the reactor to control the pH and precipitation rate. The reactor temperature, pH, and stir rate were carefully controlled throughout the reaction. After the reaction, the resultant $Ni_{0.9}Mn_{0.05}Al_{0.05}(OH)_2$ powder was washed thoroughly, vacuum-filtered, and dry overnight at 100 °C. Finally, $LiNi_{0.9}Mn_{0.05}Al_{0.05}O_2$ (NMA) was synthesized by mixing the mixed-metal hydroxide precursor with $LiOH{\cdot}H_2O$ in a molar ratio of 1:1.01 and subsequently calcining at 760 °C for 12 h under O_2 flow.

2.2. Cell fabrication and electrochemical testing

Two types of cells were constructed for the work described in this manuscript: 1) "powder-type" or pellet-cell cells which were cycled inside a pellet-press setup, and 2) coin cells which were used for electrochemical impedance spectroscopy (EIS) characterization. All cell fabrication was conducted in an argon filled glovebox with <0.1 ppm H_2O.

For powder-type cells, the catholyte consisted of 55 wt% NMA, 44 wt % chlorinated argyrodite (Ampcera Argyrodite Li_6PS_5Cl Sulfide Solid Electrolyte, Pass 325 mesh D50 < 10 um), and 1 wt% vapor grown carbon fiber (VGCF, Sigma-Aldrich DxL 100 nm × 20–200 nm). Components (~2 g) were ground in a mortar and pestle for 45 min to achieve intimate mixing. The anode consisted of 99 wt% nano-silicon (Oak Ridge National Laboratory; 230 nm diameter) [41] and 1 wt% PVDF (Solvay 5130) thin film. Xylene (Sigma-Aldrich) was added to silicon/PVDF mixture to form a slurry which was subsequently doctor-blade coated onto a copper-foil current collector (12 μm thick) at a speed of ~5 cm/s and a wet gap of 50 μm. These films were then dried in vacuum at room temperature overnight.

Cells were assembled and cycled in a custom pellet press (12 mm inner diameter) with titanium plungers and a polyether ether ketone (PEEK) body which is described in detail by Martin et al. [42] The silicon anode (5.55 mAh/cm^2 with 1C = 1500 mAh/g_{Si}) was added to the pellet press followed by ~100 mg of dry powdered LPSC which was subsequently pressed at 300 MPa to form an approximately 300 μm thick separator layer. Next, the dry powdered catholyte (56 mg or 4.9 mAh/cm^2 with 1C = 180 mAh/g_{NMA}) was then added on top of the SSE layer, pressed to 350 MPa and then slowly released to the ultimate cycling pressure of 180 MPa. Formation occurred at C/20 (1C = 180 mAh/g) charge/discharge rates between 2.9 and 4.2 *V*. Subsequent charge and discharge steps were all performed under constant current conditions at approximately C/20 or C/4, between 2.9 and 4.3 V, followed by 1-h constant-voltage holds. Cells rested for 15 min between charge and discharge. All cells were cycled at room temperature.

Coin cells (CR 2032) were fabricated for EIS measurements. The anode consisted to the same thin-film silicon described above. The separator was fabricated by first making a slurry of LPSC in xylene and doctor blade coating (200 μm wetgap) at ~5 cm/s onto a mylar film. After drying, the film was pressed onto a porous polyaramid fabric (ACP Composites) at 400 MPa to form a ~ 100 μm thick, free-standing separator [43]. The catholyte was made by adding 3 % by mass of polyisobutene binder (in a xylene solution) to the NMA, LPSC, and *V*GCF mixture (50 wt% NMA, 45 wt% LPSC, 4 wt% Oppanol, 1 wt% VGCF). Additional xylene was added to form a slurry which was doctor blade coated onto Al foil using a doctor-blade coater with wet gap of 200 μm. The final dry coating thickness was not measured. The 1st charge and discharge formation cycle were performed at a C/20 rate between 2.9 and 4.2 V with EIS interruptions every 30 min. Frequencies were swept in potentiostatic mode from 1 MHz to 10 mHz with an AC amplitude to 10 mA.

2.3. X-ray diffraction

X-ray diffraction (XRD) measurements of pre- and post-cycled powder-type pellet cells were acquired to probe changes in the crystal structure of the active material. Data was acquired using a Rigaku Smart Lab diffractometer with a D/teX Ultra 250 1D detector and Cu Kα X-ray source. All samples were prepared inside an argon glovebox and placed in an air-free holder for XRD analysis. 2-theta scans were taken using a divergence slit of one-fourth, an anti-scatter slit of 1, and a 10 mm mask.

2.4. X-ray photoelectron spectroscopy

X-ray photoelectron spectroscopy (XPS) measurements were performed using a Physical Electronics Phi VersaProbe III with monochromatic Al *Kα* X-ray excitation ($h\nu = 1.487$ keV). The instrument was calibrated to Cu $2p_{3/2}$ at 932.62 eV and Au $4f_{7/2}$ at 83.96 eV. XPS data processing and curve fitting were carried out using a custom program based on Igor Pro Software previously described [44]. The net positive charge applied to delithiate the NMA cathode during the virtual electrode X-ray photoelectron spectroscopy (VE-XPS) experiment was accomplished using UV photons (He—I, hv = 21.22 eV) supplied by a helium lamp (Physical Electronics Model 04–900). The VE-XPS method used here was described in detail by Wood et al. previously [45]. The NMA||LPSC||silicon cells were fabricated using the same method as the powder-type cells outlined above. The cells were disassembled from the custom pellet-press after was 350 MPa applied and removed for VE-XPS. Ball milling of the NMA cathodes to increase their surface area was

accomplished in a zirconia vessel with 3 mm diameter zirconia milling media in a Retsch PM 200 planetary mill at 450 rpm for 75 min as described previously [46].

2.5. Attenuated total-reflectance fourier transform infrared spectroscopy (ATR-FTIR)

A Bruker Invenio FTIR spectrometer equipped with a monolithic diamond ATR crystal and room-temperature DTGS detector was used to collect vibrational absorption spectra of dry powder cathode materials (55 wt% pristine NMA, 44 wt% LPSC, 1 wt% VGCF), uncycled NMA cathode, and cycled NMA cathode. The cycled cell was a powder-type cell described above which had undergone 25 cycles at either C/20 or C/4. To avoid exposure to air, the samples were prepared in an argon-filled glovebox (<0.1 ppm H_2O). The samples were sealed inside a coin cell cap atop the monolithic diamond ATR crystal as previously described [47]. The samples were then removed from the glovebox for FTIR measurements. IR spectra were collected with a resolution of 4 cm^{-1} and a 32-scan average.

2.6. Confocal Raman microscopy

Raman scattering spectra of the NMA and silicon interfaces with LPSC electrolyte from NMA||LPSC||silicon cells, cycled and uncycled, were acquired using a Renishaw inVia confocal Raman microscope with a 532 nm, 100 mW (RL532C100) laser source and a Leica N Plan EPI 20×/0.4NA objective. Spectra were collected in the range of 50–1835 cm^{-1} using an 1800 g/mm diffraction grating, a 532 nm notch filter, 1 % laser power, 5 s exposure time, and 12 accumulations (60 s total acquisition time).

2.7. Nanocomputed tomography

Nano X-ray computed tomography (nano CT) was used to image the catholyte both before and after being pressed to 350 MPa. The catholyte was prepared by placing the material into 100 μm outer diameter capillaries inside a glovebox. The capillaries loaded with pristine and pressed catholyte powder were imaged using a lab-based nano-CT instrument (Zeiss Xradia 810 Ultra, Carl Zeiss) with a quasi-monochromatic X-ray energy of 5.4 keV. The images were taken with a pixel binning of 2 and a pixel size of 128 nm to obtain a field of view of 64 μm × 64 μm. The catholyte samples were rotated through 180° and radiographs were collected at 0.163° intervals, resulting in a total of 1101 projections. Absorption contrast was used to image the catholyte samples. The raw radiograph images were reconstructed using a commercial software package (Reconstructor Scout-and-Scan, Carl Zeiss). The visualization of the images was carried out using Dragonfly (2022.2.0.1409, Object Research System).

3. Results and discussion

3.1. Electrochemical

The electrochemical results of a high-loading (4.9 mAh/cm^2), all-solid-state, NMA||LPSC||Si thin-film hybrid cell are shown in Fig. 1a–d. The initial discharge capacity indicates 92 % NMA utilization at C/20 discharge (1C = 180mAh/g). The differential capacity plots reveal the anticipated NMA H3 to H2 phase transition, followed by the H2 to monoclinic phase (more below). Furthermore, the CC discharge capacity of the faster C/4 rate is only 10 % less than the C/20 rate, suggesting that the cell has low overall impedance. This was confirmed with the electrochemical impedance spectroscopy (EIS) spectra seen in

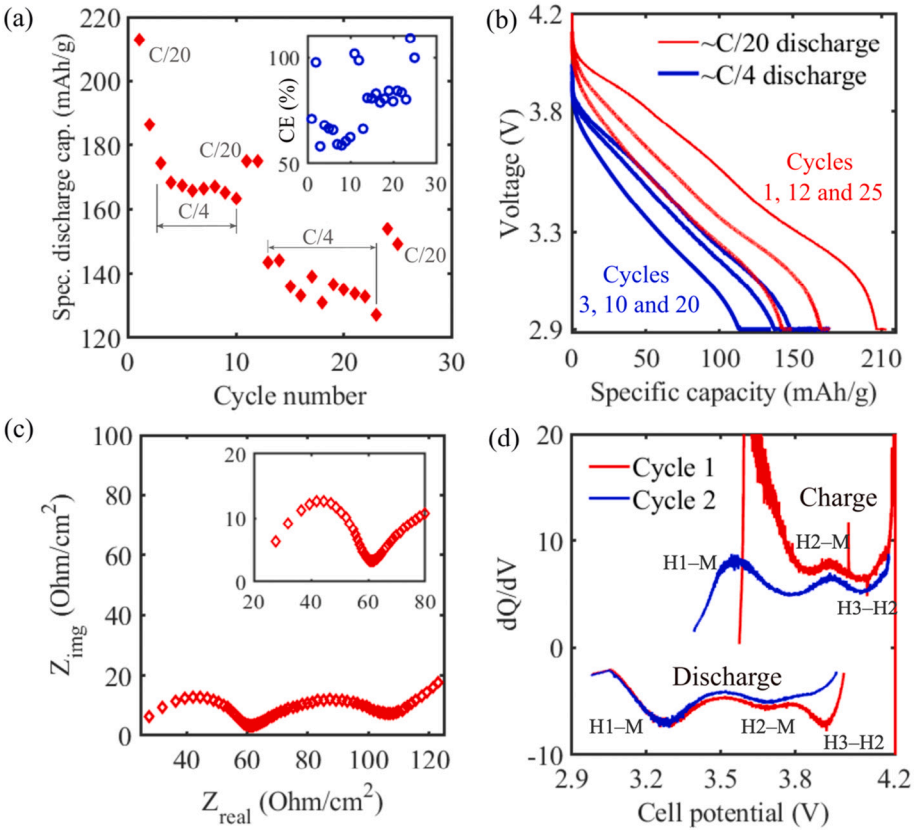

Fig. 1. a) The specific discharge capacity in mAh/g and columbic efficiency by cycle number for a 4.9 mAh/cm^2 NMA–Si cell cycled at room temperature and 180 MPa stack pressure. b) Voltage profiles and Electrochemical impedance spectroscopy (c) of the NMA–Si cell after 25 cycles showing low overall cell resistance. Inset shows high frequency region. d) Differential capacity plot for the first two cycles for the same NMA-Si cell shown in (a).

Fig. 1c taken after 10 cycles at approximately 50 % state-of-charge. An 80 % state-of-health was reached after 25 cycles. This rapid capacity fade represents a tradeoff between high initial capacity and overall capacity retention which is discussed in more detail in the characterization section to follow. This all solid-state, Ni-rich cell performs well when compared to the large range of specific discharge capacities reported in the literature (from 90 to 190 mAh/g) for similar cell chemistries, specifically, its high initial discharge of 213 mAh/g and 750 Wh/kg at room temperature [7–9].

Notably, the NMC-silicon cell exhibited a poor coulombic efficiency (CE) as shown in (Fig. 1a) despite a high first-cycle discharge capacity (213 mAh/g). The coulombic efficiency (CE) is near 100 % at C/20 but remains low (approximately 80 %) for the C/4 cycling rates without the expected decrease in the overall charge/discharge capacity (if all the CE could be attributed to active material loss or irreversible lithium inventory consumption, there would be a C/20 discharge capacity of <25 mAh/g after ten cycles.). This discrepancy – while concerning – does not prevent the cell from reaching top-of-charge voltage, having reasonable discharge capacities, and having "noisy" voltage profiles [48,49]. It can likely be attributed to soft shorting, or more specifically, transient lithium dendrites that form and degrade as the cell is cycled [31]. Three-electrode measurements for similar cell chemistries show low potentials at the silicon anode on charging—near lithium's plating potential [50] — subjecting the cell to soft short conditions. It's possible that the cell also suffers from partially reversible LPSC redox activity when in contact with electrically conductive carbon reducing its CE, reported previously [23]. A cell capable of operating at such low CEs and reasonably high capacities warrants further study outside the scope of this text.

To gain insight into the electrochemical behavior of the NMA||LPSC||Si cells, differential capacity data are analyzed (Fig. 1d) for the 1st and 2nd cycle for the cell. Typically, NMA cathodes display similar redox activity in differential capacity plots when compared to other nickel-rich NMC-type cathodes and the features of NMC-type cells containing silicon anodes are often dominated by the cathode's redox peaks [11,51,52] Oxidation peaks begin above 3.5 *V* with lithiation of silicon and NMA H1 to M phase transition (hexagonal to monoclinic phase) and then shifts from the M phase to H2 near 3.75 V and starts the H2 to H3 phase transition above 4.1 *V*. The lack of oxidation below 3.5 V on the first charge suggests that electrolyte degradation caused by high surface area carbon contact has largely been avoided [16]. The H1 to M phase transition can often present as two separate peaks, it is believed that they present as a single peak here because they are obscured by the likely significant LPSC decomposition that occurs above 2.9 *V*. While the H1 to M and M to H2 oxidation peaks can clearly be seen in Fig. 1d, only the start of the H2 to H3 phase transition can be seen in this plot because the cell underwent a voltage hold at 4.2 V (DV ~0) so it was removed for easier viewing. On reduction, the phases reverse in order and present as three peaks at 3.9, 3.7, and 3.25 V. Surprisingly, the H3 to H2 reduction peak (3.9 V) has decreased significantly from the 1st to the 2nd cycle. This may be because the voltage cutoff for the cell at this stage was 4.2 V and overpotential caused by LPSC degradation during the 1st cycle kept the cathode from fully reaching the H2 to H3 oxidation potential, evidenced by the early onset and diminished area under the H2 to H3 oxidation peak for the 2nd cycle. This, coupled with the specific discharge capacity, suggests that NMA

cathodes do not display obvious differences in electrochemical behavior compared to typical nickel-rich NMC cathodes in all solid-state cells using argyrodite electrolytes [53].

Full NMA||LPSC||Si coin cells were fabricated, and electrochemical impedance spectroscopy (EIS) was conducted as a function of state-of-charge (SoC) to gain additional information into the behavior of this system. The 1st formation cycle was performed at a C/20 rate with potentiostatic EIS interruptions every 30 min and 10-min rests. Frequencies were swept from 1 MHz to 10 mHz with an AC amplitude to of +/− 10 m*V*. Insets on each figure contain the high-frequency portions of the spectra. The EIS spectra for the 1st charge cycle have been broken down into 3 sections for ease of viewing. The 1st section corresponds to the low-voltage region (<3.5 *V*), and the 1st spectra in this panel occurred at 0.7 V (a table of voltages and SoC vs time can be seen in Fig. S1). In general, full cell solid-state batteries can be qualitatively assessed assuming processes are presented from high to low frequency as: R_{SSEb} and $R_{SSEgrain}$ which are the resistance of the bulk and grain

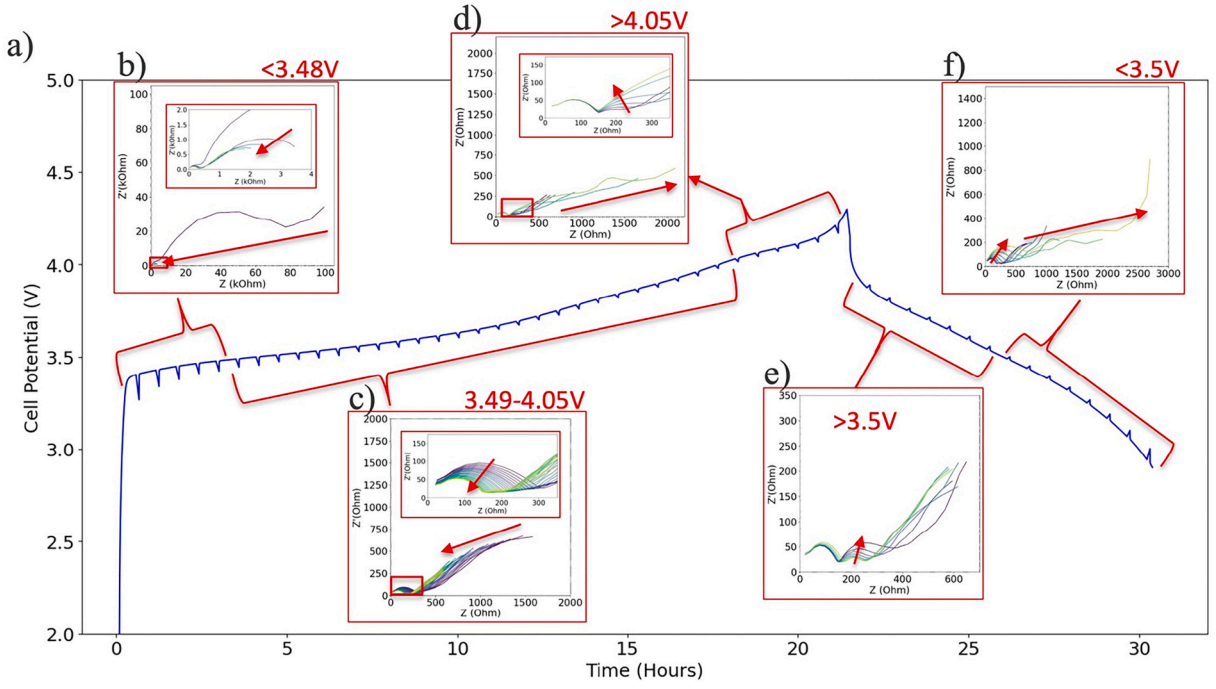

Fig. 2. Electrochemical impedance spectroscopy (EIS) plots taken during the 1st charge (c–d) and 1st discharge (e,f). Cell potential vs time plots for the 1charge and discharge (a) detail where in the charge/discharge profile the EIS plots were taken. More detailed EIS graphs can be seen in fig. S2 and S3. Additional electrochemical cycling data can be seen in Fig. S4.

boundaries of the solid-state electrolyte, R_{anode} and $R_{cathode}$ which are the resistances of the anode and cathode electrode composites, and constant phase element or Warburg element to capture diffusion into the electrodes [54].

Starting with the first charge, a large resistance of 90 kΩ is present at low cell potential (<0.75 *V*) that corresponds to pristine silicon and a fully lithiated cathode [55]. A rapid decrease in the overall cell resistance occurs quickly upon initial charging as the silicon begins to lithiate. The next EIS spectrum occurs at a cell potential of 3.40 *V* and shows a collapse of the overall cell potential to 4 kΩ. Two semicircles are present at voltages below 4.05 V. A large portion of the second semicircle (in the low frequency range) can be attributed to the pristine silicon electrode which begins to lithiate at 0.2 V vs Li which corresponds to an overall cell potential >3.4 *V* [56]. Both semicircles decrease as the SoC increases beyond 10 % from 3.55 to 4.05 V, which is common for both NMC-type cathodes and silicon anodes [57,58]. The low-frequency semicircle diminishes to reveal the Warburg tail and the high-frequency semicircle decreases from ~300 Ohm to ~150 Ohm. Above 4.05 V (70 % SoC), the high-frequency semicircle remains static, and the low-frequency peak expands and evolves into multiple features (Fig. 2d). While NMC-type cathodes have small changes (<30 Ohm/cm^2) in their resistance measured by EIS above 80 % SoC, silicon anodes do have large changes (>300 Ohm/cm^2) [58,59]. This observation suggests that the silicon anode approaches full lithiation above 4.12 *V*. This would be remarkable because the N:P ratio (ratio of the negative electrode to that of the positive) of 1.13 would make it impossible for the cathode to fully lithiate the anode alone, suggesting additional lithium was made available from LPSC degradation at the cathode [60].

The 1st discharge EIS can be seen in Fig. 2e–f. Here, the high-frequency semicircle expands slightly while the low-frequency semicircle increases to a greater extent. This remains the case until ~3.5 V is reached (54 % SoC). Below 3.5 V, both the low and the high-frequency semicircles increase in size. As the voltage decreases, the low-frequency semicircle disappears, the Warburg tail vanishes and a large semicircle with a resistance of ~2 kΩ appears. This appears similar to Fig. 2b when the voltage was 3.40 V. Much speculation exists about the physical processes at play during the 1st cycle of this NMA||LPCS||Si cell. There are aspects of the spectra that are strikingly similar to cells reported in

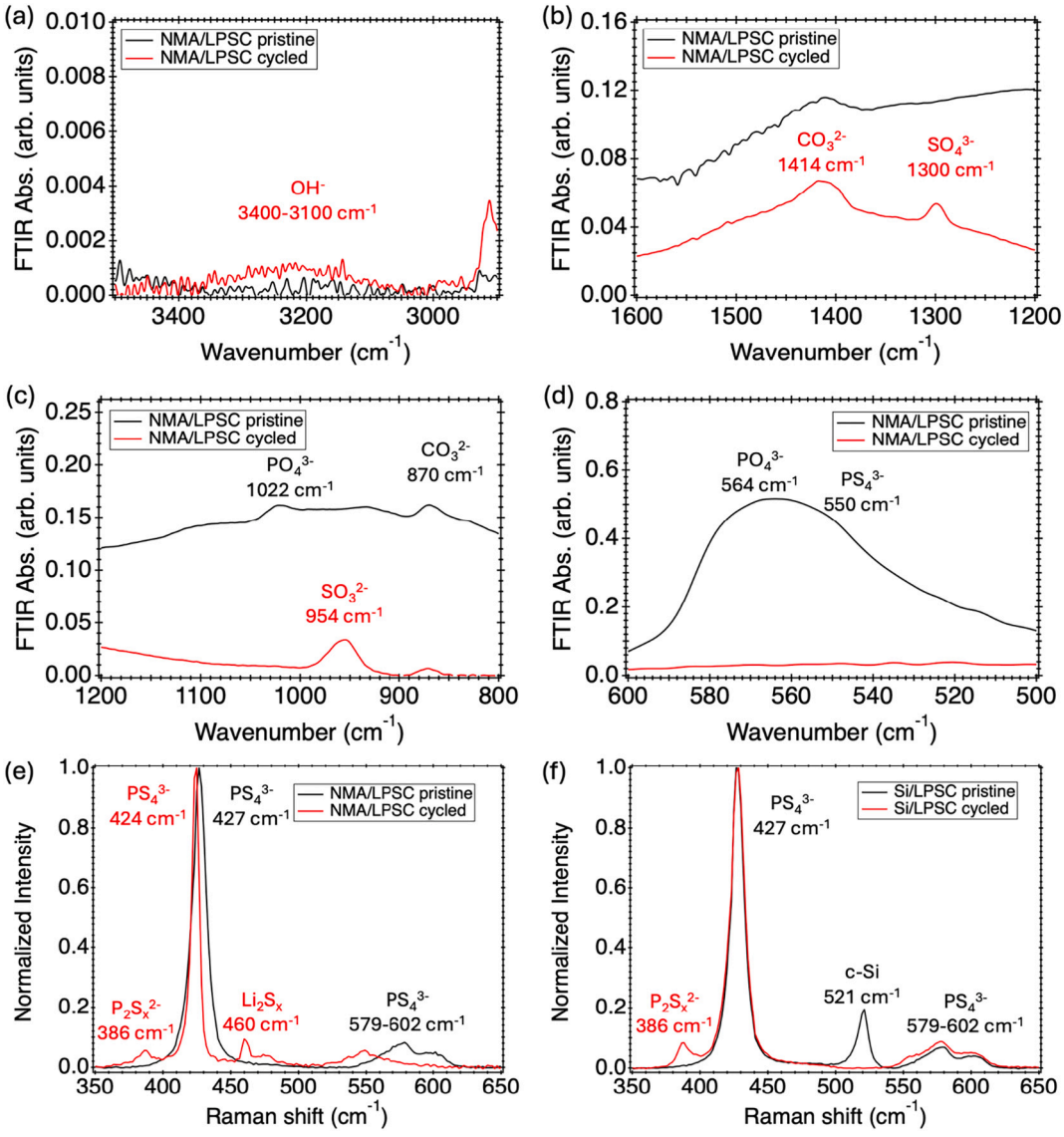

Fig. 3. Fourier Transform Infrared Spectroscopy data (a–d) showing select wavenumber ranges corresponding to the major electrolyte degradation peaks for both uncycled and cycled catholyte material containing NMA cathode and LPSC electrolyte. Raman spectra comparing pristine and cycled (e) NMA-LPSC interface and (f) Silicon-LPSC interface. Intensity has been normalized to the PS_4^{3-} stretching mode intensity at around 425 cm^{-1}. The full FTIR and Raman spectra can be seen in Fig. S5.

the literature. Ke Pan et al. performed Distribution of Relaxation Times (DRT) for several Si—Si, Li—Si and Li—Li cells in order to deconvolute different processes from the EIS data. The authors assigned DRT peaks P1, P2, and P3 to the high-frequency contact loss process, SEI diffusion process, and charge transfer kinetics, respectively. They demonstrated that the charge transfer kinetics shows the largest variation with SoC, because the charge transfer kinetics follows the Butler-Volmer equation which is strongly dependent on the lithium concentration at the Si-electrolyte interface [58]. These trends follow closely to what is reported here, and strongly suggests that the change in the low-frequency semicircle can be attributed to the change in charge transfer kinetics at the silicon anode with SoC or interfacial decomposition of the LPSC, which would introduce new charge transfer interfaces in the impedance spectra.

3.2. Fourier transform infrared spectroscopy

The FTIR spectra of cycled and uncycled NMA-LPSC catholytes (Fig. 3) show profound degradation of the LPSC electrolyte in the cycled cell. Two main degradation pathways have been identified for the LPSC SSEs, electrochemical and oxygen-involving [40]. Electrochemical degradation of the LPSC readily occurs with the most common cathode and anode pairings due to its limited electrochemical stability window (~1.07–2.01 *V*) [21]. This pathway yields degradation products such as LiCl, P_2S_5, P, and sulfur. Oxygen-involving decomposition can occur whenever there is an oxygen source available and yields degradation products like LiCl, phosphates, sulfites, and sulfates. There are several sources of oxygen available for oxidative decomposition: oxygen released from the cathode active material, organic species on the SSE material, or water absorbed to any of the cell components [40].

The absence of a broad peak near 3000 cm^{-1} (Fig. 3a) suggests that there is no water absorbed to the material. While there is no evidence of water in the material, XPS data (Fig. 5c) shows that there is indeed oxygen present in the catholyte (discussed below). The presence of sulfur oxides can be seen at 975 and 1300 cm^{-1} (Fig. 3c, b) in the cycled material. It is unclear if oxygen evolving from the NMA cathode caused the sulfate formation but there is no indication of structural reformation associated with oxygen release from NMA (discussed below). Carbonate anion asymmetric stretching (1425 cm^{-1}) and out-of-plane bending (865 cm^{-1}) can be seen in both samples, suggesting the formation Li_2CO_3 [61] or from carbonate moieties within the VGCF additive. The peak at 1030 cm^{-1} and 567 cm^{-1} represents vibration of PO_4 group that is present in the pristine material [42,62]. It is likely that the broad peak shown in the Fig. 3d uncycled spectra represents a convolution of PO_4 and PS_4 signals or some mixture of partially hydroxylated thiophosphates. This suggests that some Li_3PO_4 and Li_2CO_3, contamination may be present in the pristine material as potential the oxygen sources. The absence of the PO_4 group vibrational modes post-cycling can be attributed to different stoichiometric ratios of other LPSC decomposition products such as S_xO, P_2S_5 and LiCl-related species which can reduce the number of phosphates present [40].

Although FTIR measurements show a disappearance of the PS_4^{3-} argyrodite moiety upon cycling, more-sensitive Raman scattering spectra of the catholyte (Fig. 3e) shows persistence of the this chemical group symmetric vibration but with a shift to lower energies from 427 to 424 cm^{-1} and 580 to 550 cm^{-1} upon cycling [63]. Also evident in the cycled sample spectrum are $Li_2S_{x>2}$ LPSC decomposition products at 460 cm^{-1}. A small peak ~475 cm^{-1} can be attributed to S—S dimers can be seen in the cycled catholyte but not at the anode [64].

The silicon anode interface with the LPSC was also characterized by Raman (Fig. 3f). The pristine sample shows a clear peak of crystalline silicon at 521 cm^{-1} that is not existent after cycling. This indicates lithiation of the silicon occurred during charging and amorphous silicon was formed after discharging. The broad amorphous silicon peak expected around 470 cm^{-1} in the cycled sample is likely obscured by the strong PS_4^{3-} stretching mode absorption at 427 cm^{-1}. Also noticeable in the cycled spectrum is evidence of LPSC degradation into $P_2S_x^{2-}$ with a peak at 386 cm^{-1}, like what was found at the catholyte.

3.3. X-ray diffraction

To probe the crystal structure of the cathode material after cycling, X-ray diffraction data was collected for both uncycled catholyte and catholyte that had seen 25 cycles of 2.8–4.3 *V*. The sample that had seen electrochemical cycling was fully discharged (NMA fully lithiated) before being disassembled in an argon filled glovebox and placed into an air-free holder. The Rigaku SmartLab system contained a Cu *Kα* X-ray source.

The results are plotted in Fig. 4. The diffractogram of the silicon anode can be seen in Fig. 4a. The 111, 220, and 311 peaks of crystalline silicon can be seen for the uncycled material. Upon cycling, the silicon amorphized and its XRD peaks disappear with only the peaks of the Cu substrate visible. This suggests that although the N:P ratio for the cell was 1.13, much of the silicon was lithiated in the course of 25 cycles.

The diffractogram of the catholyte demonstrates a phase pure NMA cathode consistent with that found in the literature [11] and appears to remain highly crystalline after cycling as evidenced by the splitting of the 018/110 peaks [65]. Although the NMA in both samples is fully lithiated, peak shifts in the 003, 101, 104, and 018/110 peaks suggest that lithium has been consumed in the cell. The peak shifts expected of a

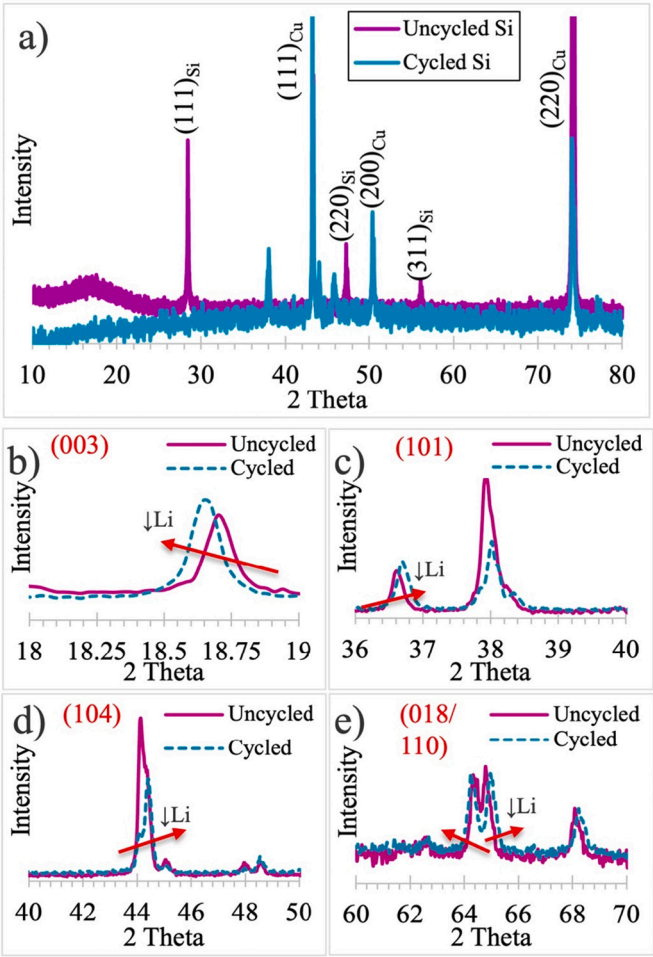

Fig. 4. X-ray diffraction data showing the diffractogram for both the silicon (a) and catholyte (b-e) sides of a NMA–silicon solid-state pellet before cycling (uncycled) and post-cycling (cycled). Panels b-e show the prominent peaks of the NMA active material and suggest that lithium loss has occurred after cycling. The full 2 theta range for the catholyte can be seen in Fig. S6.

partially delithiated NMA-type cathode material are denoted in the figure with red arrows. This suggests that a non-trivial amount of lithium loss occurred after 25 cycles which, as discussed above, could be the formation of dead lithium (from hard or soft shorts) that is encouraged to form at the high cycling pressures used in this study [30], lithium irreversibly bound in the silicon anode as trapped lithium which can account for ~40 % of the lithium loss in Li—Si cells, or the conversion of LPSC into higher lithium content stoichiometries such as, Li_2S, Li_3P, or LiCl as we have reported previously [66].

3.4. X-ray photoelectron spectroscopy (XPS)

To further probe the NMA-argyrodite interface, X-ray photoelectron spectroscopy (XPS) spectra were taken of 5 samples (Fig. 5). XPS studies were either conducted ex-situ (Fig. 5e–h) or via virtual electrode X-ray photoelectron spectroscopy (*VE*-XPS in Fig. 5a–d) which has been used to study other solid-state systems and described previously [42,45].

The samples for the VE-XPS (Fig. 5a–d) were prepared identically to the powder-type hybrid cells in Fig. 1. The catholyte of the powder-type cells was illuminated with a UV light source to liberate electrons, thus creating a positive charge, which delithiates the NMA particles. The spectral series is taken as the charge in the cathode increases, with the pristine spectra at the bottom. The ex-situ samples (Fig. 5e–h) contain uncycled and cycled catholyte mixtures that have NMA in one of two morphologies, pristine and ball-milled. The purpose of the ball milling is to maintain the chemistry of the NMA while increasing its surface area

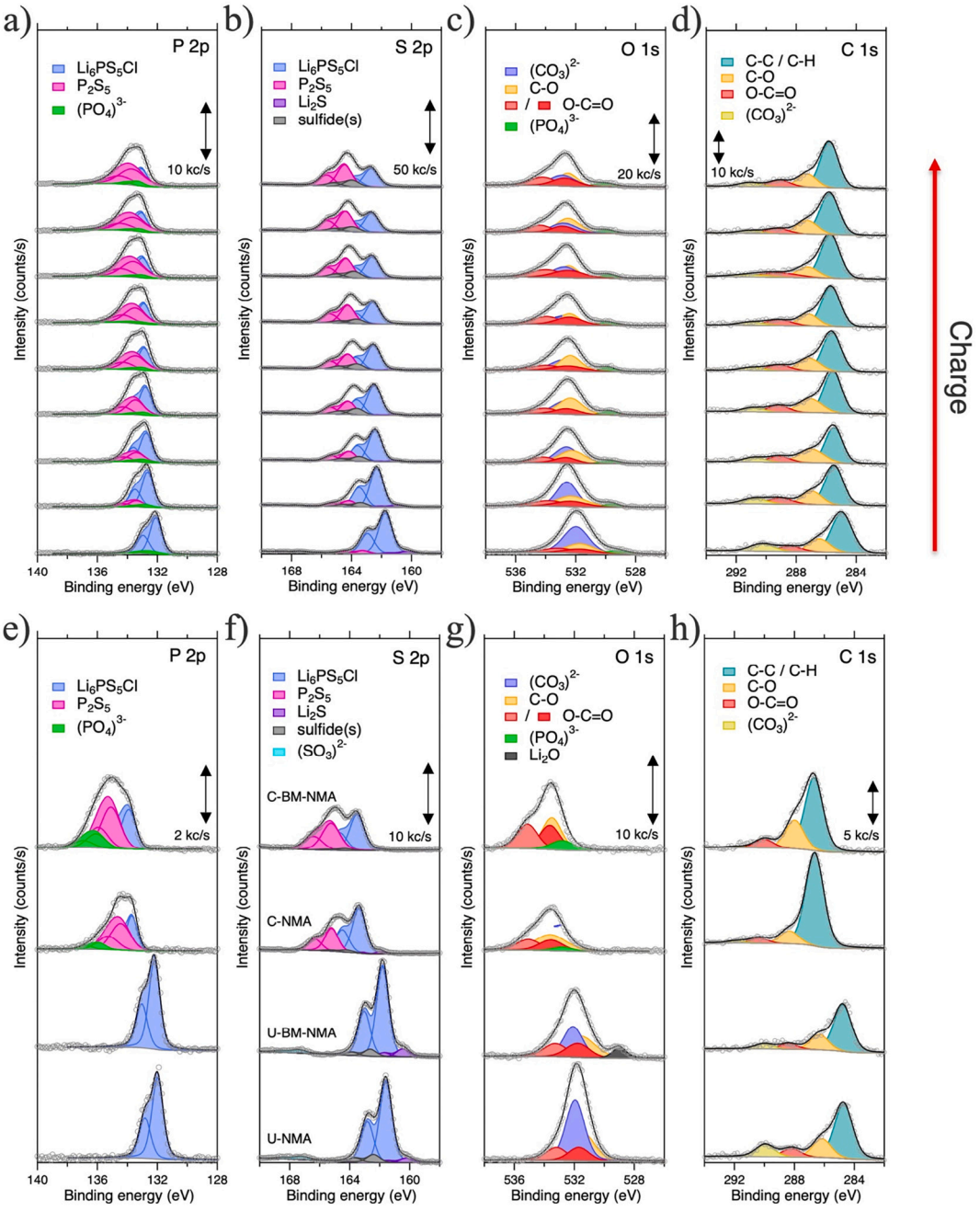

Fig. 5. A VE-XPS experiment on the NMA portion of a NMA vs Si ASSB (a–d). The series shows increasing charge with the pristine catholyte at the bottom. Ex-situ X-ray photoelectron spectroscopy data showing spectra from both cycled (C-NMA) and uncycled (U-NMA) catholyte for the P2p, S2p, O1s, and C1s (e–h) binding energies. Samples names with "BM" signify catholyte materials that contain NMA particles that were ball milled to increase their surface area-to-volume ratio before being mixed with LPSC and carbon. XPS data of pristine NMA powder can be seen in Fig. S7.

and thus the NMA-argyrodite interface. The NMA was milled according to the method described previously [46]. The uncycled material is denoted as U-NMA. NMA that had been ball-milled before it was formed into a catholyte is denoted U-BM-NMA. Catholyte material that had been cycled for one cycle at a rate of C/20 between 2.9 and 4.3 V is denoted C-NMA and C-BM-NMA.

The XPS spectra show that the argyrodite SSE is nearly pristine before cycling. The binding energies for the P2p, S2p, O1s, and C1s (Fig. 5) spectra are consistent with Li_6PS_5Cl and there was no discernable change in the Cl 2p signal [67]. This includes oxygen contamination present in the pristine argyrodite [68]. The pristine material seems to contain at least some phosphate before cycling in agreement with the FTIR data shown above. The pristine sample also shows evidence of residual Li_2S precursor which recedes on cycling (Fig. 5b, f). After cycling, the cathode–SSE interface decomposes into expected phases: P_2S_x, uncharged sulfur species, and phosphates [67]. Ball-milling results in more phosphates at the cathode–SSE interface than the untreated sample, which is likely due to the higher surface area. The areas of the phosphate peaks in the P2p (135.7 eV) and O1s (535.0 eV) core levels are >3× larger than the untreated sample, suggesting that this process indeed occurs at the cathode–SSE interface and that oxygen from the NMA surface may play a role as in other nickel-rich NMC-type cathodes [69,70].

One phenomenon to highlight is the disappearance of the carbonate anion from Li_2CO_3 (Fig. 5c, g). Specifically, the carbonate anion diminishes on cycling while the other oxygen containing species remain unaffected. Interestingly, this corresponds to the increasing signal strength of the phosphate species (Fig. 5a, e). This suggests that the oxygen source for phosphate formation on cycling may be carbonates from either the argyrodite or the NMA surfaces (Fig. S7). There is a slight discrepancy between the FTIR and XPS data on this matter that may be attributed to the difference in penetration depth between the methods. Interestingly, there appears to be some phase segregation of the degradation products when examining cross-sectional images of cycled pellet cells with energy-dispersive X-ray spectroscopy (Fig. S8). These images suggest that there may be some migration of degradation species which could lead to differences in spectroscopic data when comparing results from methods with different penetration depths. The contaminant Li_2O peak disappears after cycling in the ball-milled sample. As the cathode–SSE interface degrades during cycling, these phases either decompose or are covered up by the new phases that form. It is difficult to tell from this data, but additional experiments may reveal both the exact mechanism of their disappearance and the connection between carbonate anions and phosphate and/or sulfate formation. If the formation of phosphate is indeed caused by the decomposition of lithium carbonate, it should be accompanied by the release of carbon monoxide or dioxide species. There is some evidence in the literature as to the origin of uncharged (—S0— groups) sulfur species. Anion polysulfide formation (P–[S]*n*–P-type) with increasing values of *n,* or the number of bridging sulfur atoms, will have increasing number of uncharged sulfur species that will result in the doublet at higher binding energies that depend on the polysulfide chain length [28]. Almost all of the degradation species discussed here contribute to overall cell resistance, except for possibly the phosphate species. Several approaches may be considered to limit cathode–SSE degradation, including mixed SEE species to make stable interfaces with lithium metal, LiF-Li_3N protective layers, and AgI alloy inducing films [71–73].

3.5. Nanocomputed tomography

Cross-sections of pre- and post-consolidated catholyte powders are shown in Fig. 6. In these images, lighter colors represent higher X-ray attenuation coefficients. Hence, NMA particles appear white due to their higher effective atomic number (and therefor higher attenuation coefficient) in comparison to LPSC particles or pores which are dark grey and not sufficiently resolved by this diagnostic. The pre-consolidation NMA particles seen in Fig. 6a–d are generally round with the expected size distribution (approximately 10 μm.). In contrast, severe cracking or fracturing is observed (yellow dashed circles) in the NMA particles of the post-consolidation catholyte (Fig. 6e–i) [46]. The fracture of the secondary structure of the NMA particles is similar to the fracturing that occurs when calendering electrodes to low-porosity (<30 %) which can cause decrease capacity retention [74]. While calandering can exert pressures >50 MPa, much higher pressures are routinely used to consolidate ASSBs [75]. Hence, it is reasonable to assume that mechanical damage to active material particles is prevalent across various catholyte compositions when high consolidation-pressures are used. Fabrication pressures typically used for pellet-type cells in the literature exceed 300 MPa and are most likely inflicting significant damage the secondary structure of the nickel-rich cathodes. The results from the nano CT indicate that fabrication pressures must be limited to prevent cathode fracturing. New methods for catholyte consolidation may be

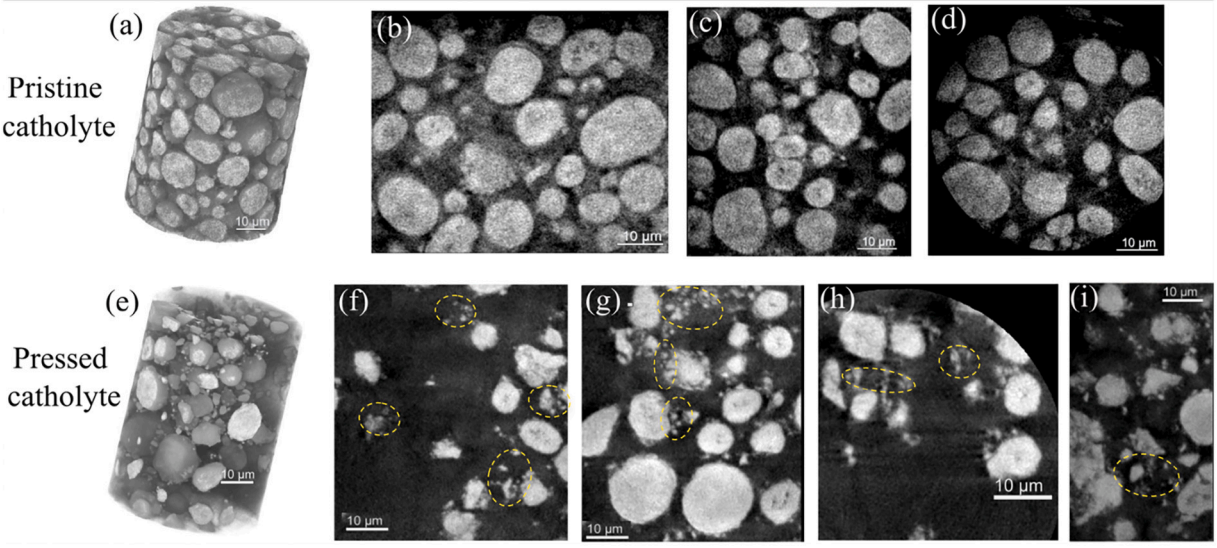

Fig. 6. Nanocomputed tomography images showing cross-sections of catholyte materials (a–d) and catholyte materials that had been pressed to the fabrication pressure of 350 MPa (e–i). The NMA particles are shown in white and appear spherical in the unpressed sample (a–d) and fractured (yellow dashed circle) in the pressed sample (e–i). (For interpretation of the references to colour in this figure legend, the reader is referred to the web version of this article.)

necessary to produce films that limit cathode cracking while achieving ionic conductivities that mostly require high fabrication pressures at this moment.

4. Conclusion

A high-loading (~5 mAh/cm^2) all-solid-state pellet cell containing a no-cobalt NMA cathode and 99 wt% silicon anode has been reported for the first time. This cell had an impressive initial discharge capacity at room temperature >210 mAh/g_{NMA} at C/20 charge/discharge rate and 178 mAh/g_{NMA} when cycled at a rate of C/4. Electrolyte degradation closely resembled that of other nickel-rich transition metal oxide cathode materials, suggesting the NMA does not cause superfluous electrolyte degradation. The argyrodite solid electrolyte degrades via electrochemical and oxygen-involving pathways in our experiments. Specifically, it is shown the carbonate anion from Li_2CO_3 on the NMA or argyrodite surface may be the oxygen source for phosphate formation for the first time. The NMA cathode shows extensive fracturing after the application of the 350 MPa fabrication pressure. Future studies should limit oxygen contamination on the surface of cathodes or in the solid electrolyte that may promote electrolyte degradation and decrease capacity retention. Careful consideration should be applied when choosing fabrication pressures for pellet-type cells. The high fabrication pressures commonly used for bench-scale experiments can lead to extensive cathode active material particle fracture which can lead to dramatic capacity fade. It's critical for studies to more thoroughly explore the balance between achieving intimate contact between the cathode active material and the electrolyte, and the risk of damaging the active material through excessive pressure.

Funding

This work was authored in part by the National Renewable Energy Laboratory (NREL), operated by Alliance for Sustainable Energy, LLC, for the U.S. Department of Energy (DOE) under Contract No. DE-AC36-08GO28308. Funding provided by the U.S. Department of Energy's Vehicle Technologies Office (VTO) under the Low-Pressure All-Solid-State Cells project directed by Simon Thompson and Tien Duong and managed by Anthony Burrell. The views expressed in the article do not necessarily represent the views of the DOE or the U.S. Government. The U.S. Government retains and the publisher, by accepting the article for publication, acknowledges that the U.S. Government retains a nonexclusive, paid-up, irrevocable, worldwide license to publish or reproduce the published form of this work, or allow others to do so, for U.S. Government purposes.

Notes

The authors declare the following competing financial interest(s): One of the authors (A. M.) is a co-founder of TexPower, Inc., a start-up company focusing on cobalt-free cathode materials for lithium-based batteries.

CRediT authorship contribution statement

Ryan Brow: Writing – review & editing, Writing – original draft, Visualization, Methodology, Investigation, Formal analysis, Data curation, Conceptualization. **Zachary Berquist:** Writing – review & editing, Formal analysis, Data curation. **Steven Lee:** Writing – original draft, Data curation. **Trevor Martin:** Writing – review & editing, Writing – original draft, Formal analysis, Data curation, Conceptualization. **Lydia Meyer:** Writing – review & editing, Writing – original draft, Data curation. **Maxwell Schulze:** Writing – review & editing, Writing – original draft, Visualization, Formal analysis, Data curation, Conceptualization. **Avtar Singh:** Writing – review & editing, Writing – original draft, Visualization, Methodology, Formal analysis, Data curation, Conceptualization. **Ryan Tancin:** Writing – review & editing, Writing – original draft, Formal analysis. **Glenn Teeter:** Visualization, Methodology, Formal analysis, Data curation. **Gabriel Veith:** Writing – review & editing, Formal analysis, Data curation. **Bertrand J. Tremolet de Villers:** Writing – review & editing, Writing – original draft, Visualization, Formal analysis, Data curation. **Andrew Colclasure:** Writing – review & editing, Project administration, Methodology, Funding acquisition, Formal analysis, Conceptualization. **Arumugam Manthiram:** Supervision, Project administration, Investigation, Data curation.

Declaration of competing interest

The authors declare the following financial interests/personal relationships which may be considered as potential competing interests: Ryan Brow reports financial support was provided by National Renewable Energy Laboratory. Ryan Brow reports financial support was provided by Vehicle Technologies Office. Arumugam Manthiram reports a relationship with TexPower Inc. that includes: board membership and equity or stocks. If there are other authors, they declare that they have no known competing financial interests or personal relationships that could have appeared to influence the work reported in this paper.

Data availability

Data will be made available on request.

Acknowledgments

This work was authored in part by the National Renewable Energy Laboratory (NREL), operated by Alliance for Sustainable Energy, LLC, for the U.S. Department of Energy (DOE) under Contract No. DE-AC36-08GO28308. This work was supported by the U.S. Department of Energy. This research was supported by the U.S. Department of Energy's Vehicle Technologies Office under the Advanced Battery Materials Research (BMR) Program, directed by Simon Thompson and Tien Duong. The views expressed in the article do not necessarily represent the views of the DOE or the U.S. Government. The U.S. Government retains and the publisher, by accepting the article for publication, acknowledges that the U.S. Government retains a nonexclusive, paid-up, irrevocable, worldwide license to publish or reproduce the published form of this work, or allow others to do so, for U.S. Government purposes.

Appendix A. Supplementary data

Supplementary data to this article can be found online at https://doi.org/10.1016/j.est.2024.113329.

References

[1] Albertus, Paul, Venkataramani Anandan, Chunmei Ban, Nitash Balsara, Ilias Belharouak, Josh Buettner-Garrett, Zonghai Chen, et al. "Challenges for and pathways toward Li-metal-based all-solid-state batteries." ACS Energy Letters 6, no. 4 (2021/04/09 2021): 1399–404. doi:https://doi.org/10.1021/acsenergylett.1c00445.

[2] Wang, Changhong, and Xueliang Sun. "The Promise of Solid-State Batteries for Safe and Reliable Energy Storage." Engineering 21 (2023/02/01/2023): 32–35. doi: 10.1016/j.eng.2022.10.008. https://www.sciencedirect. com/science/article/pii/S2095809922007664.

[3] Sovacool, Benjamin K. "The precarious political economy of cobalt: balancing prosperity, poverty, and brutality in artisanal and industrial Mining in the Democratic Republic of the Congo." The Extractive Industries and Society 6, no. 3 (2019/07/01/2019): 915–39. doi:https://doi.org/10.1016/j.exis.2019.05.018. https://www.sciencedirect. com/science/article/pii/S2214790X1930084X.

[4] Li, Matthew, and Jun Lu. "Cobalt in Lithium-ion batteries." Science 367, no. 6481 (2020/02/28 2020): 979–80. doi:https://doi.org/10.1126/science.aba9168. doi: 10.1126/science.aba9168.

[5] Yu, Chuang, Feipeng Zhao, Jing Luo, Long Zhang, and Xueliang Sun. "Recent development of Lithium Argyrodite solid-state electrolytes for solid-state batteries:

synthesis, structure, stability and dynamics." Nano Energy 83 (2021/05/01/2021): 105858. doi:https://doi.org/10.1016/j.nanoen.2021.105858. https://www.sciencedirect. com/science/article/pii/S2211285521001166.

[6] Nie, Kaihui, Yanshuai Hong, Jiliang Qiu, Qinghao Li, Xiqian Yu, Hong Li, and Liquan Chen. "interfaces between cathode and electrolyte in solid state Lithium batteries: challenges and perspectives." [in English]. Review. Frontiers in Chemistry 6 (2018-December-12 2018). doi:https://doi.org/10.3389/fchem.2018.00616. https://www. frontiersin.org/articles/https://doi.org/10.3389/fchem.2018.00616.

[7] Tsukasaki, Hirofumi, Yota Mori, Misae Otoyama, So Yubuchi, Takamasa Asano, Yoshinori Tanaka, Takahisa Ohno, et al. "Crystallization behavior of the Li2s–P2s5 glass electrolyte in the Lini1/3mn1/3co1/3o2 positive electrode layer." Sci. Rep. 8, no. 1 (2018/04/18 2018): 6214. doi:https://doi.org/10.1038/s41598-018-24524-7. doi:10.1038/s41598-018-24524-7.

[8] Subramanian, Yuvaraj, Rajesh Rajagopal, and Kwang-Sun Ryu. "Synthesis, Air Stability and Electrochemical Investigation of Lithium Superionic Bromine Substituted Argyrodite (Li6-Xps5-Xcl1.0brx) for All-Solid-State Lithium Batteries." Journal of Power Sources 520 (2022/02/01/2022): 230849. doi:https://doi.org/10.1016/j.jpowsour.2021. 230849. https://www.sciencedirect.com/science/article/pii/S0378775321013379.

[9] Chen, Ting, Long Zhang, Zhaoxing Zhang, Peng Li, Hongqiang Wang, Chuang Yu, Xinlin Yan, Limin Wang, and Bo Xu. "Argyrodite solid electrolyte with a stable Interface and superior dendrite suppression capability realized by Zno co-doping." ACS Appl. Mater. Interfaces 11, no. 43 (2019/10/30 2019): 40808–16. doi: https://doi.org/10.1021/acsami.9b13313. doi:10.1021/acsami.9b13313.

[10] Ryu, Hoon-Hee, Been Namkoong, Jae-Hyung Kim, Ilias Belharouak, Chong S. Yoon, and Yang-Kook Sun. "Capacity fading mechanisms in Ni-rich single-crystal Ncm cathodes." ACS Energy Letters 6, no. 8 (2021/08/13 2021): 2726–34. doi:https://doi.org/10.1021/acsenergylett.1c01089. doi:10.1021/acsenergylett.1c01089.

[11] Li, Wangda, Steven Lee, and Arumugam Manthiram. "High-Nickel Nma: A Cobalt-Free Alternative to Nmc and Nca Cathodes for Lithium-Ion Batteries." Advanced Materials 32, no. 33 (2020/08/01 2020): 2002718. doi:10. 1002/adma.202002718. doi:https://doi.org/10.1002/adma.202002718.

[12] Wenzel, Sebastian, Stefan J. Sedlmaier, Christian Dietrich, Wolfgang G. Zeier, and Juergen Janek. "Interfacial reactivity and interphase growth of Argyrodite solid electrolytes at Lithium metal electrodes." Solid State Ion. 318 (2018/05/01/2018): 102–12. doi:https://doi.org/10.1016/j.ssi.2017.07.005. https://www.sciencedirect.com/science/ article/pii/S0167273817301200.

[13] Sun, Lin, Yanxiu Liu, Rong Shao, Jun Wu, Ruiyu Jiang, and Zhong Jin. "Recent Progress and future perspective on practical silicon anode-based Lithium ion batteries." Energy Storage Materials 46 (2022/04/01/2022): 482–502. doi:https://doi.org/10.1016/j.ensm.2022.01.042. https://www.sciencedirect.com/science/article/pii/S2405829722000496.

[14] Ping, Weiwei, Chunpeng Yang, Yinhua Bao, Chengwei Wang, Hua Xie, Emily Hitz, Jian Cheng, Teng Li, and Liangbing Hu. "A silicon anode for garnet-based all-solid-state batteries: interfaces and Nanomechanics." Energy Storage Materials 21 (2019/09/01/2019): 246–52. doi:https://doi.org/10.1016/j.ensm.2019.06.024. https://www. sciencedirect.com/science/article/pii/S2405829719308463.

[15] Liu, Hongbin, Qing Sun, Hongqiang Zhang, Jun Cheng, Yuanyuan Li, Zhen Zeng, Shuai Zhang, et al. "The application road of silicon-based anode in Lithium-ion batteries: from liquid electrolyte to solid-state electrolyte." Energy Storage Materials 55 (2023/01/01/2023): 244–63. doi:https://doi.org/10.1016/j.ensm.2022.11.054. https://www.sciencedirect.com/science/article/pii/S2405829722006547.

[16] Tan, Darren H. S., Yu-Ting Chen, Hedi Yang, Wurigumula Bao, Bhagath Sreenarayanan, Jean-Marie Doux, Weikang Li, et al. "Carbon-free high-loading silicon anodes enabled by sulfide solid electrolytes." Science 373, no. 6562 (2021/09/24 2021): 1494–99. doi:https://doi.org/10.1126/science.abg7217. doi: 10.1126/science.abg7217.

[17] Deiseroth, Hans-Jörg, Shiao-Tong Kong, Hellmut Eckert, Julia Vannahme, Christof Reiner, Torsten Zaiß, and Marc Schlosser. "Li6ps5x: a class of crystalline Li-rich solids with an unusually high Li+ mobility." Angew. Chem. Int. Ed. 47, no. 4 (2008/01/11 2008): 755–58. doi:https://doi.org/10.1002/anie.200703900. doi: 10.1002/anie.200703900.

[18] Rao, R. P., and S. Adams. "Studies of Lithium Argyrodite Solid Electrolytes for All-Solid-State Batteries." physica status solidi (a) 208, no. 8 (2011/08/01 2011): 1804–07. doi:https://doi.org/10.1002/pssa.201001117. doi:10.1002/pssa.201001117.

[19] Jiang, Yidong, Anjie Lai, Jun Ma, Kai Yu, Huipeng Zeng, Guangzhao Zhang, Wei Huang, et al. "Fundamentals of the cathode-electrolyte Interface in all-solid-state Lithium batteries." ChemSusChem 16, no. 9 (2023/05/05 2023): e202202156. doi: https://doi.org/10.1002/cssc.202202156. doi:10.1002/cssc.202202156.

[20] Koerver, Raimund, Isabel Aygün, Thomas Leichtweiß, Christian Dietrich, Wenbo Zhang, Jan O. Binder, Pascal Hartmann, Wolfgang G. Zeier, and Jürgen Janek. "Capacity fade in solid-state batteries: interphase formation and Chemomechanical processes in nickel-rich layered oxide cathodes and Lithium thiophosphate solid electrolytes." Chem. Mater. 29, no. 13 (2017/07/11 2017): 5574–82. doi:https://doi.org/10.1021/acs.chemmater.7b00931. doi:10.1021/acs.chemmater.7b00931.

[21] Zhu, Yizhou, Xingfeng He, and Yifei Mo. "Origin of outstanding stability in the Lithium solid electrolyte materials: insights from thermodynamic analyses based on first-principles calculations." ACS Appl. Mater. Interfaces 7, no. 42 (2015/10/28 2015): 23685–93. doi:https://doi.org/10.1021/acsami.5b07517. doi:10.1021/acsami.5b07517.

[22] Mayo, Martin, Kent J. Griffith, Chris J. Pickard, and Andrew J. Morris. "Ab Initio Study of Phosphorus Anodes for Lithium- and Sodium-Ion Batteries." Chemistry of Materials 28, no. 7 (2016/04/12 2016): 2011–21. doi:10. 1021/acs.chemmater.5b04208. doi:https://doi.org/10.1021/acs.chemmater.5b04208.

[23] Tan, Darren H. S., Erik A. Wu, Han Nguyen, Zheng Chen, Maxwell A. T. Marple, Jean-Marie Doux, Xuefeng Wang, et al. "Elucidating Reversible Electrochemical Redox of Li6ps5cl Solid Electrolyte." ACS Energy Letters 4, no. 10 (2019/10/11 2019): 2418–27. doi:https://doi.org/10.1021/acsenergylett.9b01693. doi:https://doi.org/10.1021/acsenergylett.9b016 93.

[24] Narayanan, Sudarshan, Ulderico Ulissi, Joshua S. Gibson, Yvonne A. Chart, Robert S. Weatherup, and Mauro Pasta. "effect of current density on the solid electrolyte interphase formation at the Lithium|Li6ps5cl Interface." nature Communications 13, no. 1 (2022/11/24 2022): 7237. doi:https://doi.org/10.1038/s41467-022-34855-9. doi:10.1038/s41467-022-34855-9.

[25] Otto, Svenja- K., Luise M. Riegger, Till Fuchs, Sven Kayser, Pascal Schweitzer, Simon Burkhardt, Anja Henss, and Jürgen Janek. "In Situ Investigation of Lithium Metal–Solid Electrolyte Anode Interfaces with Tof-Sims." Advanced Materials Interfaces 9, no. 13 (2022/05/01 2022): 2102387. doi:https://doi.org/10.1002/admi.202102387. doi:10. 1002/admi.202102387.

[26] Raimund Koerver, Felix Walther, Isabel Aygün, Joachim Sann, Christian Dietrich, Wolfgang G. Zeier, Jürgen Janek, "redox-active cathode interphases in solid-state batteries." 10.1039/C7TA07641J, J. Mater. Chem. A 5 (43) (2017) 22750–22760, https://doi.org/10.1039/C7TA07641J.

[27] Jung, Sung-Kyun, Hyeokjo Gwon, Seok-Soo Lee, Hyunseok Kim, Jae Cheol Lee, Jae Gwan Chung, Seong Yong Park, Yuichi Aihara, and Dongmin Im. "Understanding the Effects of Chemical Reactions at the Cathode–Electrolyte Interface in Sulfide Based All-Solid-State Batteries." https://doi.org/10.1039/C9TA08517C. J. Mater. Chem. A 7, no. 40 (2019): 22967–76. doi:https://doi.org/10.1039/C9TA08517C. doi:10.1039/C9TA08517C.

[28] Walther, Felix, Raimund Koerver, Till Fuchs, Saneyuki Ohno, Joachim Sann, Marcus Rohnke, Wolfgang G. Zeier, and Jürgen Janek. "Visualization of the interfacial decomposition of composite cathodes in Argyrodite-based all-solid-state batteries using time-of-flight secondary-ion mass spectrometry." Chem. Mater. 31, no. 10 (2019/05/28 2019): 3745–55. doi:https://doi.org/10.1021/acs.chemmater.9b00770. doi:10.1021/acs. (chemmater.9b00770).

[29] Ke, Xinyou, Yan Wang, Liming Dai, and Chris Yuan. "Cell failures of all-solid-state Lithium metal batteries with inorganic solid electrolytes: Lithium dendrites." Energy Storage Materials 33 (2020/12/01/2020): 309–28. doi:https://doi.org/10.1016/j.ensm.2020.07.024. https://www.sciencedirect.com/science/article/pii/S2405829720302890.

[30] Cao, Daxian, Kena Zhang, Wei Li, Yuxuan Zhang, Tongtai Ji, Xianhui Zhao, Ercan Cakmak, et al. "Nondestruc- tively Visualizing and Understanding the Mechano-Electro-Chemical Origins of "Soft Short" and "Creeping" in All-Solid-State Batteries." Advanced Functional Materials 33, no. 52 (2023/12/01 2023): 2307998. doi:10.10 02/adfm.202307998. doi:https://doi.org/10.1002/adfm.202307998.

[31] Counihan, Michael J., Kanchan S. Chavan, Pallab Barai, Devon J. Powers, Yuepeng Zhang, Venkat Srinivasan, and Sanja Tepavcevic. "The phantom menace of dynamic soft-shorts in solid-state battery research." Joule 8, no. 1 (2024/01/17/2024): 64–90. doi:https://doi.org/10.1016/j.joule.2023.11.007. https://www.sciencedirect.com/science/ article/pii/S2542435123004816.

[32] McBrayer, Josefine D., Christopher A. Apblett, Katharine L. Harrison, Kyle R. Fenton, and Shelley D. Minteer. "Mechanical studies of the solid electrolyte interphase on anodes in Lithium and Lithium ion batteries." Nanotechnology 32, no. 50 (2021/09/27 2021): 502005. doi:https://doi.org/10.1088/1361-6528/ac17fe. doi:10.1088/1361-6528/ac17fe.

[33] Singh, Dheeraj Kumar, Anja Henss, Boris Mogwitz, Ajay Gautam, Jonas Horn, Thorben Krauskopf, Simon Burkhardt, et al. "Li6ps5cl microstructure and influence on dendrite growth in solid-state batteries with Lithium metal anode." cell reports physical Science 3, no. 9 (2022/09/21/2022): 101043. doi:https://doi.org/10.1016/j. xcrp.2022.101043. https://www.sciencedirect.com/science/article/pii/S266638642200337X.

[34] Narayanan, Sudarshan, Ulderico Ulissi, Joshua S. Gibson, Yvonne A. Chart, Robert S. Weatherup, and Mauro Pasta. "effect of current density on the solid electrolyte interphase formation at the Lithium|Li6ps5cl Interface." nature Communications 13, no. 1 (2022/11/24 2022): 7237. doi:https://doi.org/10.1038/s41467-022-34855-9. doi:10.1038/s41467-022-34855-9.

[35] Yang, Haodong, and Zhanjiang Wang. "Effects of pressure, temperature, and plasticity on Lithium dendrite growth in solid-state electrolytes." J. Solid State Electrochem. 27, no. 10 (2023/10/01 2023): 2607–18. doi:https://doi.org/10.1007/s10008-023-05560-4. doi:10.1007/s10008-023-05560-4.

[36] Tron, Artur, Raad Hamid, Ningxin Zhang, Andrea Paolella, Paul Wulfert-Holzmann, Vladislav Kolotygin, Pedro López-Aranguren, and Alexander Beutl. "Film Processing of Li6ps5cl Electrolyte Using Different Binders and Their Combinations." Journal of Energy Storage 66 (2023/08/30/2023): 107480. doi:https://doi.org/10.1016/j.est.2023.107 480. https://www.sciencedirect.com/science/article/pii/S2352152X23008770.

[37] Ruhl, Justine, Luise M. Riegger, Michael Ghidiu, and Wolfgang G. Zeier. "Impact of solvent treatment of the superionic Argyrodite Li6ps5cl on solid-state battery performance." Advanced Energy and Sustainability Research 2, no. 2 (2021/02/01 2021): 2000077. doi:https://doi.org/10.1002/aesr.202000077. doi:10.1002/aesr.202000077.

[38] Randrema, Xavier, Ivan Leteyi Mfiban, Marine Soler, Irina Profatilova, Manon Berthault, Raphael Ramos, Julien Lavie, et al. "Towards a practical use of sulfide solid electrolytes in solid-state batteries: impact of dry room exposure on H2s release and material properties." Batteries & Supercaps 7, no. 1 (2024/01/01 2024): e20230 0380. doi:https://doi.org/10.1002/batt.202300380. doi:10.1002/batt.202300380.

[39] Scharmann, Timon, Canel Özcelikman, Do Minh Nguyen, Carina Amata Heck, Christian Wacker, Peter Michalowski, Arno Kwade, and Klaus Dröder. "Quantification of hydrogen sulfide development during the production of all-solid-state batteries with Argyrodite sulfide-based separators." ACS Applied Energy Materials 7, no. 3 (2024/02/12 2024): 1261–69. doi:https://doi.org/10.1021/acsaem.3c02888. doi:10.1021/acsaem.3c02888.

[40] Zuo, Tong-Tong, Felix Walther, Jun Hao Teo, Raffael Rueß, Yubo Wang, Marcus Rohnke, Daniel Schröder, Linda F. Nazar, and Jürgen Janek. "Impact of the chlorination of Lithium Argyrodites on the electrolyte/ cathode Interface in solid-state batteries." Angew. Chem. Int. Ed. 62, no. 7 (2023/02/06 2023): e202213228. doi:https://doi.org/10.1002/anie.202213228. doi:10.1002/anie.202213228.

[41] Araño, Khryslyn G., Beth L. Armstrong, Ethan Boeding, Guang Yang, Harry M. Meyer, III, Evelyna Wang, Rachel Korkosz, et al. "Functionalized Silicon Particles for Enhanced Half- and Full-Cell Cycling of Si-Based Li-Ion Batteries." ACS Applied Materials & Interfaces 15, no. 8 (2023/03/01 2023): 10554–69. doi:10.1021/acsami.2c16978. doi:https://doi.org/10.1021/acsami.2c16978.

[42] Martin, Trevor R., Glenn Teeter, Chun-Sheng Jiang, and Kyusung Park. "Sulfur polymers as flexible interfacial additives for low stack-pressure solid-state Lithium-ion batteries." Batteries Supercaps 6, no. 10 (2023/10/ 01 2023): e202300255. doi:https://doi.org/10.1002/batt.202300255. doi:10.1002/batt.202300255.

[43] Xu, Ruochen, Jie Yue, Sufu Liu, Jiangping Tu, Fudong Han, Ping Liu, and Chunsheng Wang. "Cathode-Supported All-Solid-State Lithium–Sulfur Batteries with High Cell-Level Energy Density." ACS Energy Lett. 4, no. 5 (2019/05/10 2019): 1073–79. doi:https://doi.org/10.1021/acsenergylett.9b00430. doi:10.1021/acsenergylett.9b00430.

[44] Wood, Kevin N., and Glenn Teeter. "Xps on Li-battery-related compounds: analysis of inorganic Sei phases and a methodology for charge correction." ACS Applied Energy Materials 1, no. 9 (2018/09/24 2018): 4493–504. doi:https://doi.org/10.1021/acsaem.8b00406. doi:10.1021/acsaem.8b00406.

[45] Wood, Kevin N., K. Xerxes Steirer, Simon E. Hafner, Chunmei Ban, Shriram Santhanagopalan, Se-Hee Lee, and Glenn Teeter. "operando X-ray photoelectron spectroscopy of solid electrolyte interphase formation and evolution in Li2s-P2s5 solid-state electrolytes." nature Communications 9, no. 1 (2018/06/27 2018): 2490. doi:https://doi.org/10.1038/s41467-018-04762-z. doi:10.1038/s41467-018-04762-z.

[46] Brow, Ryan, Anthony Donakowski, Alex Mesnier, Drew J. Pereira, K. Xerxes Steirer, Shriram Santhanagopalan, and Arumugam Manthiram. "Mechanical pulverization of co-free nickel-rich cathodes for improved high-voltage cycling of Lithium-ion batteries." ACS Applied Energy Materials 5, no. 6 (2022/06/27 2022): 6996–7005. doi:https://doi.org/10.1021/acsaem.2c00606. doi:10.1021/acsaem.2c00606.

[47] Meyer, Lydia, David Curran, Ryan Brow, Shriram Santhanagopalan, and Jason Porter. "Operando measurements of electrolyte Li-ion concentration during fast charging with Ftir/Atr." J. Electrochem. Soc. 168, no. 9 (2021/09/06 2021): 090502. doi:https://doi.org/10.1149/1945-7111/ac1d7a. doi:10.1149/1945-7111/ac1d7a.

[48] Homann, Gerrit, Lukas Stolz, Jijeesh Nair, Isidora Cekic Laskovic, Martin Winter, and Johannes Kasnatscheew. "Poly(ethylene oxide)-based electrolyte for solid-state-Lithium-batteries with high voltage positive electrodes: evaluating the role of electrolyte oxidation in rapid cell failure." Sci. Rep. 10, no. 1 (2020/03/09 2020): 4390. doi:https://doi.org/10.1038/s41598-020-61373-9. doi:10.1038/s41598-020-61373-9.

[49] Wang, Changhong, Tao Deng, Xiulin Fan, Matthew Zheng, Ruizhi Yu, Qingwen Lu, Hui Duan, et al. "Identifying soft breakdown in all-solid-state Lithium battery." Joule 6, no. 8 (2022/08/17/2022): 1770–81. doi:https://doi.org/10.1016/j.joule.2022.05.020. https://www.sciencedirect.com/science/article/pii/S2542435122002471.

[50] Fan, Zengjie, Bing Ding, Zhiwei Li, Zhi Chang, Ben Hu, Chong Xu, Xingyu Zhang, Hui Dou, and Xiaogang Zhang. "In-situ Prelithiation of electrolyte-free silicon anode for sulfide all-solid-state batteries." eTransportation 18 (2023/10/01/2023): 100277. doi:https://doi.org/10.1016/j.etran.2023.100277. https://www.sciencedirect. com/science/article/pii/S2590116823000528.

[51] Maxwell C. Schulze, Fernando Urias, Nikita S. Dutta, Zoey Huey, Jaclyn Coyle, Glenn Teeter, Ryan Doeren, et al., "control of nanoparticle dispersion, Sei composition, and electrode morphology enables long cycle life in high silicon content nanoparticle-based composite anodes for Lithium-ion batteries." 10.1039/D2TA089 35A, J. Mater. Chem. A 11 (10) (2023) 5257–5266, https://doi.org/10.1039/D2TA08935A (doi:10.1039/ D2TA08935A).

[52] Zhang, Yan, Bisai Li, Bin Tang, Zeen Yao, Xiongjie Zhang, Zhifeng Liu, Runlong Gong, and Pengpeng Zhao. "Mechanical Constraining Double-Shell Protected Si-Based Anode Material for Lithium-Ion Batteries with Long-Term Cycling Stability." Journal of Alloys and Compounds 846 (2020/12/15/2020): 156437. doi:10. 1016/j.jallcom.2020.156437. https://www.sciencedirect.com/science/article/pii/S0925838820328012.

[53] Kitsche, David, Yushu Tang, Yuan Ma, Damian Goonetilleke, Joachim Sann, Felix Walther, Matteo Bianchini, Jürgen Janek, and Torsten Brezesinski. "High Performance All-Solid-State Batteries with a Ni-Rich Ncm Cathode Coated by Atomic Layer Deposition and Lithium Thiophosphate Solid Electrolyte." ACS Applied Energy Materials 4, no. 7 (2021/07/26 2021): 7338–45. doi:https://doi.org/10.1021/acsaem.1c01487. doi:https://doi.org/10.1021/acsaem. 1c01487.

[54] Vadhva, Pooja, Ji Hu, Michael J. Johnson, Richard Stocker, Michele Braglia, Dan J. L. Brett, and Alexander J. E. Rettie. "Electrochemical Impedance Spectroscopy for All-Solid-State Batteries: Theory, Methods and Future Outlook." ChemElectroChem 8, no. 11 (2021/06/01 2021): 1930–47. doi:https://doi.org/10.1002/celc.202100108. doi:10.10 02/celc.202100108.

[55] Lozhkina, D. A., A. M. Rumyantsev, and E. V. Astrova. "Impedance spectroscopy of porous silicon and silicon-carbon anodes produced by sintering." Semiconductors 54, no. 3 (2020/03/01 2020): 383–91. doi:https://doi.org/10.1134/S1063782620030124. doi:10.1134/S1063782620030124.

[56] Cangaz, Sahin, Felix Hippauf, Florian Steffen Reuter, Susanne Doerfler, Thomas Abendroth, Holger Althues, and Stefan Kaskel. "Enabling High-Energy Solid-State Batteries with Stable Anode Interphase by the Use of Columnar Silicon Anodes." Advanced Energy Materials 10, no. 34 (2020/09/01 2020): 2001320. doi:10.1002/aenm.202001320. doi:https://doi.org/10.1002/aenm.202001320.

[57] Xiao, Haiqing, Ziqiang Tao, Hong Bai, Hongwei Wang, Yanling Fu, Nianpeng Si, and Hua Bai. "State of charge effects on the parameters of electrochemical impedance spectroscopy equivalent circuit model for Lithium ion batteries." IOP Conference Series: Earth and Environmental Science 474, no. 5 (2020/04/01 2020): 052038. doi:https://doi.org/10.1088/1755-1315/474/5/052038. doi:10.1088/1755-1315/474/5/052038.

[58] Pan, Ke, Feng Zou, Marcello Canova, Yu Zhu, and Jung-Hyun Kim. "Comprehensive electrochemical Impe- dance spectroscopy study of Si-based anodes using distribution of relaxation times analysis." J. Power Sources 479 (2020/12/15/2020): 229083. doi:https://doi.org/10.1016/j.jpowsour.2020.229083. https://www.science- direct.com/science/article/pii/S0378775320313781.

[59] Moškon, Jože, Jan Žuntar, Sara Drvarič Talian, Robert Dominko, and Miran Gaberšček. "A powerful transmission line model for analysis of impedance of insertion battery cells: a case study on the Nmc-Li system." J. Electrochem. Soc. 167, no. 14 (2020/11/12 2020): 140539. doi:https://doi.org/10.1149/1945-7111/abc769. doi:10.1149/1945-7111/abc769.

[60] Morino, Yusuke, Hirofumi Tsukasaki, and Shigeo Mori. "Microscopic Degradation Mechanism of Argyrodite-Type Sulfide at the Solid Electrolyte–Cathode Interface." ACS Appl. Mater. Interfaces 15, no. 19 (2023/05/17 2023): 23051–57. doi:https://doi.org/10.1021/acsami.3c00462. doi:10.1021/acsami.3c00462.

[61] Yu-Ting Chen, Maxwell A.T. Marple, Darren H.S. Tan, So-Yeon Ham, Baharak Sayahpour, Wei-Kang Li, Hedi Yang, et al., "investigating dry room compatibility of sulfide solid-state electrolytes for scalable manufacturing." 10.1039/D1TA09846B, J. Mater. Chem. A 10 (13) (2022) 7155–7164, https://doi.org/10.1039/D1TA09846B.

[62] Benoy, Santhi Maria, Shraddha Singh, Mayank Pandey, and Manoj B. "Characterization of Nanocarbon based electrode material derived from anthracite coal." Materials Research Express 6, no. 12 (2020/01/08 2019): 125624. doi:https://doi.org/10.1088/2053-1591/ab619d. doi:10.1088/2053-1591/ab619d.

[63] Wang, Longlong, Ayan Mukherjee, Chang-Yang Kuo, Sankalpita Chakrabarty, Reut Yemini, Arrelaine A. Dameron, Jaime W. DuMont, et al. "High-energy all-solid-state Lithium batteries enabled by co-free Linio2 cathodes with robust outside-in structures." Nat. Nanotechnol. 19, no. 2 (2024/02/01 2024): 208–18. doi:https://doi.org/10.1038/s41565-023-01519-8. doi:10.1038/s41565-023-01519-8.

[64] Yubuchi, So, Miwa Uematsu, Minako Deguchi, Akitoshi Hayashi, and Masahiro Tatsumisago. "Lithium-Ion-Conducting Argyrodite-Type Li6ps5x (X = Cl, Br, I) Solid Electrolytes Prepared by a Liquid-Phase Technique Using Ethanol as a Solvent." ACS Applied Energy Materials 1, no. 8 (2018/08/27 2018): 3622–29. doi:10.1021/ acsaem.8b00280. doi:https://doi.org/10.1021/acsaem.8b00280.

[65] Park, Nam-Yung, Geon-Tae Park, Su-Bin Kim, Wangmo Jung, Byung-Chun Park, and Yang-Kook Sun. "Degradation mechanism of Ni-rich cathode materials: focusing on particle interior." ACS Energy Letters 7, no. 7 (2022/07/08 2022): 2362–69. doi:https://doi.org/10.1021/acsenergylett.2c01272. doi:10.1021/acsenergylett.2c01272.

[66] Li, Yuchen, Xueying Zheng, Zhang Cao, Yan Wang, Yueyue Wang, Linze Lv, Weibo Huang, Yunhui Huang, and Honghe Zheng. "Unveiling the mechanisms into Li-trapping induced (Ir)reversible capacity loss for silicon anode." Energy Storage Materials 55 (2023/01/01/2023): 660–68. doi:https://doi.org/10.1016/j.ensm.2022.12.032. https://www.sciencedirect.com/science/article/pii/S2405829722006894.

[67] Auvergniot, Jérémie, Alice Cassel, Dominique Foix, Virgine Viallet, Vincent Seznec, and Rémi Dedryvère. "Redox activity of Argyrodite Li6ps5cl electrolyte in all-solid-state Li-ion battery: an Xps study." Solid State Ion. 300 (2017/02/01/2017): 78–85. doi:https://doi.org/10.1016/j.ssi.2016.11.029. https://www.sciencedirect.com/ science/article/pii/S0167273816307512.

[68] Jung, Wo Dum, Minjae Jeon, Sung Soo Shin, Ji-Su Kim, Hun-Gi Jung, Byung-Kook Kim, Jong-Heun Lee, Yong-Chae Chung, and Hyoungchul Kim. "functionalized sulfide solid electrolyte with air-stable and chemical-resistant Oxysulfide Nanolayer for all-solid-state batteries." ACS Omega 5, no. 40 (2020/10/13 2020): 26015–22. doi:https://doi.org/10.1021/acsomega.0c03453. doi:10.1021/acsomega.0c03453.

[69] Kobayashi, Shunsuke, Hideaki Watanabe, Takeharu Kato, Fuminori Mizuno, and Akihide Kuwabara. "Atomic-Scale Observations of Oxygen Release Degradation in Sulfide-Based All-Solid-State Batteries with Layered Oxide Cathodes." ACS Applied Materials & Interfaces 14, no. 34 (2022/08/31 2022): 39459–66. doi:10.10 21/acsami.2c06950. doi:https://doi.org/10.1021/acsami.2c06950.

[70] Ando, Keisuke, Tomoyuki Matsuda, Takuya Miwa, Mitsumoto Kawai, and Daichi Imamura. "Degradation Mechanism of All-Solid-State Lithium-Ion Batteries with Argyrodite Li7−Xps6−Xclx Sulfide through High-Temperature Cycling Test." Battery Energy 2, no. 3 (2023/05/01 2023): 20220052. doi:https://doi.org/10.1002/bte2.2022 0052. doi:https://doi.org/10.1002/bte2.20220052.

[71] Li, Shuai, Shi-Jie Yang, Gui-Xian Liu, Jiang-Kui Hu, Yu-Long Liao, Xi-Long Wang, Rui Wen, et al. "A Dynamically Stable Mixed Conducting Interphase for All-Solid-State Lithium Metal Batteries." Advanced Materials 36, no. 3 (2024/01/01 2024): 2307768. doi:https://doi.org/10.1002/adma.202307768. doi:https://doi.org/10.1002/adma.2023 07768.

[72] Wu, Ming, Mengqi Li, Yuming Jin, Xinshuang Chang, Xiaolei Zhao, Zhi Gu, Gaozhan Liu, and Xiayin Yao. "in situ formed Lif-Li3n Interface layer enables ultra-stable sulfide electrolyte-based all-solid-state Lithium batteries." journal of energy Chemistry 79 (2023/04/01/2023): 272–78. doi:https://doi.org/10.1016/j.jechem.2023.01.007. https://www.sciencedirect.com/science/article/pii/S209549562300013X.

[73] Liao, Yu-Long, Jiang-Kui Hu, Zhong-Heng Fu, Chen-Zi Zhao, Yang Lu, Shuai Li, Shi-Jie Yang, et al. "Integra- ted Interface Configuration by in-Situ Interface Chemistry Enabling Uniform Lithium Deposition in All-Solid-State Lithium Metal Batteries." Journal of Energy Chemistry 80 (2023/05/01/2023): 458–65. doi:10.1016/j.jechem.2023.02.012. https://www.sciencedirect.com/science/article/pii/S2095495623001018.

[74] Sim, Richard, Steven Lee, Wangda Li, and Arumugam Manthiram. "Influence of Calendering on the Electrochemical Performance of Lini0.9mn0.05al0.05o2 Cathodes in Lithium-Ion Cells." ACS Applied Materials & Interfaces 13, no. 36 (2021/09/15 2021): 42898–908. doi:https://doi.org/10.1021/acsami.1c12543. doi:10. 1021/acsami.1c12543.

[75] Zhang, Fengyu, Yunna Guo, Liqiang Zhang, Peng Jia, Xiang Liu, Ping Qiu, Hongbing Zhang, and Jianyu Huang. "A review of the effect of external pressure on all-solid-state batteries." eTransportation 15 (2023/01/01/ 2023): 100220. doi:https://doi.org/10.1016/j.etran.2022.100220. https://www.sciencedirect.com/science/article/pii/S259011 6822000650.